Bound single-particle states and scattering of nucleons on spherical nuclei with a global optical model

B. Morillon and P. Romain
Commissariat à l'Énergie Atomique, DAM/DIF/DPTA/SPN, Boîte Postale 12, F-91680 Bruyères-le-Châtel, France
(Received 23 March 2007; revised manuscript received 3 July 2007; published 3 October 2007)

We present a global spherical optical model for nucleons with incident energies up to 200 MeV containing dispersive terms and a local energy approximation. This optical model was built from our previous neutron optical model and is able to reproduce scattering data as well as bound single-particle states for neutrons and protons. However, for the scattering of protons, the situation is not as satisfactory as for neutrons.

DOI: 10.1103/PhysRevC.76.044601 PACS number(s): 24.10.Ht, 21.10.Pc

I. INTRODUCTION

Recently, we succeeded in building a global neutron optical model potential (OMP) [1] including dispersion relations [2] and the local energy approximation of Perey-Buck [3]. Then, we extended it to the negative energy region toward the shell-model potential for $E < 0$ (bound states) [4]. This new global neutron OMP provides a very good description of the scattering of neutrons by spherical nuclei over a very broad energy domain (1 keV to 200 MeV) as well as of the bound single-particle states for neutrons. Because we obtained good results with this OMP, we decided to extend it for incident protons. This is exactly the purpose of this paper.

Section II provides a short description of our previous dispersive OMP for neutrons. In Sec. III we present proton bound single-particle states and proton cross sections calculated with this OMP including the Coulomb potential and the Z/R term. We explain how we succeeded in building a new nucleon OMP in Sec. IV, starting from our neutron potential. A second version of the potential is proposed with a Lane-consistent imaginary surface potential. Comparisons are made between the calculated and experimental proton and neutron cross sections (Sec. V) as well as bound single-particle states (Sec. VI). Finally, Sec. VII contains our conclusions.

II. OPTICAL MODEL

To build a nucleon OMP for spherical nuclei we start from our previous neutron OMP [1,4] written as

$$U(r,E) = [V_V(E) + iW_V(E)]f(r,R,a) - 4a[V_S(E) + iW_S(E)]\frac{df(r,R,a)}{dr} - [V_{SO}(E) + iW_{SO}(E)] \times \left(\frac{\hbar}{m_\pi c}\right)^2 \frac{1}{r}\frac{df(r,R,a)}{dr}\,\mathbf{l}.\boldsymbol{\sigma}, \quad (1)$$

where f is a Woods-Saxon form factor with radius R and diffuseness a, both independent of energy. The energy dependence of the imaginary volume (W_V) and spin-orbit (W_{SO}) terms is taken to be the form suggested by Brown and Rho [5] whereas the surface imaginary term (W_S) is a Brown-Rho shape modified by an exponential falloff. The energy dependence of the real surface part (V_S) is deduced from the imaginary surface term owing to the dispersion relations [2] and the real volume part (V_V) is defined by the local energy approximation of Perey-Buck [3] plus the dispersive contribution from the imaginary volume term. The real spin-orbit potential (V_{SO}) is defined as an exponential function and is also connected to the imaginary spin-orbit potential by a dispersion relation. This potential can be easily used with the ECIS code [6], which includes the calculation of the dispersive contributions. All the parameters needed to describe the energy dependencies for this potential can be found in Refs. [1] and [4]. When we had built our potential, we did not include the analyzing power angular distributions $A_y(\theta)$ in the χ^2 search. However, we had checked that our new global OMP provides a good description of the analyzing powers, as illustrated in Fig. 1.

III. NEUTRON OPTICAL MODEL APPLIED TO PROTONS

The simplest way to obtain a proton OMP from a neutron OMP is to add the Coulomb term produced by a uniformly charged sphere [7]:

$$V_C(r) = \frac{Ze^2}{2R_C}\left(3 - \frac{r^2}{R_C^2}\right) \quad \text{for} \quad r \leqslant R_C$$
$$= \frac{Ze^2}{r} \quad \text{for} \quad r > R_C,$$

where Z is the charge of the target and R_C is the Coulomb radius. To calculate the bound single-particle states, the reaction, and the angular distributions for protons, we have to solve the Schrödinger equation with the Coulomb potential. For this purpose, we add the Coulomb functions from the ECIS code [6] and the calculation of the proton elastic differential cross sections as well as the proton analyzing powers to the NUCLEON code [1]. The only extra parameter is the Coulomb radius R_C, which is chosen equal to that of the nuclear radius used in our previous neutron potential in a first approximation ($R_C = rA^{1/3}$, where r is the reduced radius of our potential; see Table I). The proton optical model is now specified and the first results for the proton bound single-particle states and selected proton scattering cross sections are now presented.

TABLE I. Energy dependencies and parameters for the global nucleon potential "M.R.07a". It is to be noted that the volume dispersive contribution (ΔV_V) and the surface dispersive potential ($V_S = \Delta V_S$) are not repeated here. The z term represents the charge of the projectile.

$W_S^{n,p}(E) = \frac{A_S(E-E_F^{n,p})^2}{(E-E_F^{n,p})^2+B_S^2} \exp[-C_S(E-E_F^{n,p})]$		
	neutron	proton
A_S	$-17.5 + 19\frac{N-Z}{A}$	$-17.5 - 19\frac{N-Z}{A}$
B_S	13	18.2
C_S	0.025	$0.027 - 7\,10^{-5}A$
$W_V^{n,p}(E) = \frac{A_V(E-E_F^{n,p})^2}{(E-E_F^{n,p})^2+B_V^2}$		
	neutron and proton	
A_V	$-11.21 - 0.017A$	
B_V	$62 + 0.15A$	
$W_{SO}^{n,p}(E) = \frac{-1.5(E-E_F^{n,p})^2}{(E-E_F^{n,p})^2+50^2}$		
	neutron and proton	
$V_V(E) = V_{V\,H.F.} \exp\{-\mu\beta^2/2\hbar^2\,[E - V_V(E)]\}$ $\times \exp\{+4\mu^2\gamma^2/\hbar^4\,[E - V_V(E)]^2\} + 1.15zZ/R$		
	neutron and proton	
$V_{V\,H.F.}$	-82.8	
β	1.114	
γ	$0.1165 - 10^{-4}A$	
$V_{SO}(E) = V_{SO\,H.F.} \exp\{-\mu\beta^2/2\hbar^2\,[E - V_{H.F.}(E)]\}$ $\times \exp\{+4\mu^2\gamma^2/\hbar^4\,[E - V_{H.F.}(E)]^2\}$		
	neutron and proton	
$V_{SO\,H.F.}$	-6.5	
	neutron and proton	
r	$1.3 - 2.7\,10^{-4}A$	
a	$0.566 + 5\,10^{-9}A^3$	

A. Proton bound single-particle states

The single-particle and hole state energies calculated with the real part of this OMP (including, of course, the dispersive contributions deduced from the imaginary potentials) are shown in Fig. 2 for ^{208}Pb, ^{90}Zr, and ^{40}Ca. The experimental energies of the various single-particle and hole states for those three nuclei, labeled "Exp." in Fig. 2, can be found in Refs. [8–10], respectively. For each nucleus, the left column, labeled "M.R.04 + 1/r," displays the value calculated from this proton potential. The sequential ordering of the states is rather good for ^{90}Zr and ^{40}Ca even though it is not possible to obtain the two first-particle states for ^{90}Zr, and there is poor agreement between data and calculations. However, the single-particle and hole states calculated for ^{208}Pb are completely different from experimental energies. To improve the agreement between theory and experiment, we add to the factor $V_V(E)$ a Z/R term ($R = rA^{1/3}$) to increase the depth of the real potential. This term is similar to the $0.4Z/A^{1/3}$ term used by Perey [7]. The single-particle and hole proton states predicted with this modified potential are shown in Fig. 2 (over the heading "M.R.04+1/r + Z/R"). This potential produces a clear improvement.

B. Reaction and selected scattering cross sections

The reaction cross section (left panel) and selected elastic angular distributions (right panel) for protons on ^{208}Pb calculated with the "M.R.04 + 1/r" potential (blue long-dashed lines) are compared with experimental data (black circles) in Fig. 3. The calculated reaction cross section underestimates the experimental data widely and the calculated angular distributions are not in phase with the experimental ones. The results obtained with the "M.R.04 + 1/r + Z/R" potential are shown in Fig. 3 by the red dashed-dotted lines. The discrepancy between the calculated and the experimental reaction cross section decreases but the discrepancy between the calculated and the experimental elastic angular distributions increases. However, it should be noted that the angular distributions calculated with this new potential are now nearly in phase with the experimental data. We have tried to modify the Coulomb radius R_C and to apply a coefficient different from one for the Z/R term with the two potentials ("M.R.04 + 1/r" and "M.R.04 + 1/r + Z/R"), but the results were not much closer to the experimental data.

IV. NEW OPTICAL MODEL

In the light of these first results, the real potential must be deeper for negative and positive energy to improve the agreement between the calculated and the experimental proton data. We sought new parameters for the local energy approximation in the real volume potential to avoid the Z/R term. However, it was not possible to find parameters that increase the real volume potential by about 10 MeV (for ^{208}Pb) and to avoid convergence problems in the iterative process (see Eq. (7) of Ref. [1]). For this reason, we keep the Z/R term in the proton potential and we did not modify the parameters of our previous real volume potential. In our past study of the neutron single-particle and hole states [4], we had found better agreement with the experimental levels when the real spin-orbit potential was deeper. Following this remark and to unify the different terms of the potential we have used the local energy approximation of Perey-Buck to define the real spin-orbit potential. The nonlocality ranges β and γ are exactly the same as for the real volume potential ($\beta = 1.114$ fm and $\gamma = 0.1165 - 10^{-4}A$ fm [1,4]) but the depth $V_{SO\,H.F.}$ is chosen to obtain a better agreement between theory and experiment ($V_{SO\,H.F.} = -6.5$ MeV). Energy dependencies of the depths of the old ("M.R.04") and new ("M.R.07") real spin-orbit potentials (with and without the dispersive contribution ΔV_{SO}) are shown in Fig. 4. This new real spin-orbit potential does not modify the calculated neutron analyzing powers, as one can see in Fig. 1. The reaction and elastic differential cross sections for protons on ^{208}Pb calculated with this new real spin-orbit potential are compared with experimental data and previous potentials (black dotted line) in Fig. 3. There is a clear improvement beyond 100 MeV but the calculated reaction cross section is still much lower than the experimental data. Because the calculated differential cross sections are larger than the experiments and consequently the calculated reaction cross section is smaller than the experiments, we might try to modify the imaginary part of the potential without changing

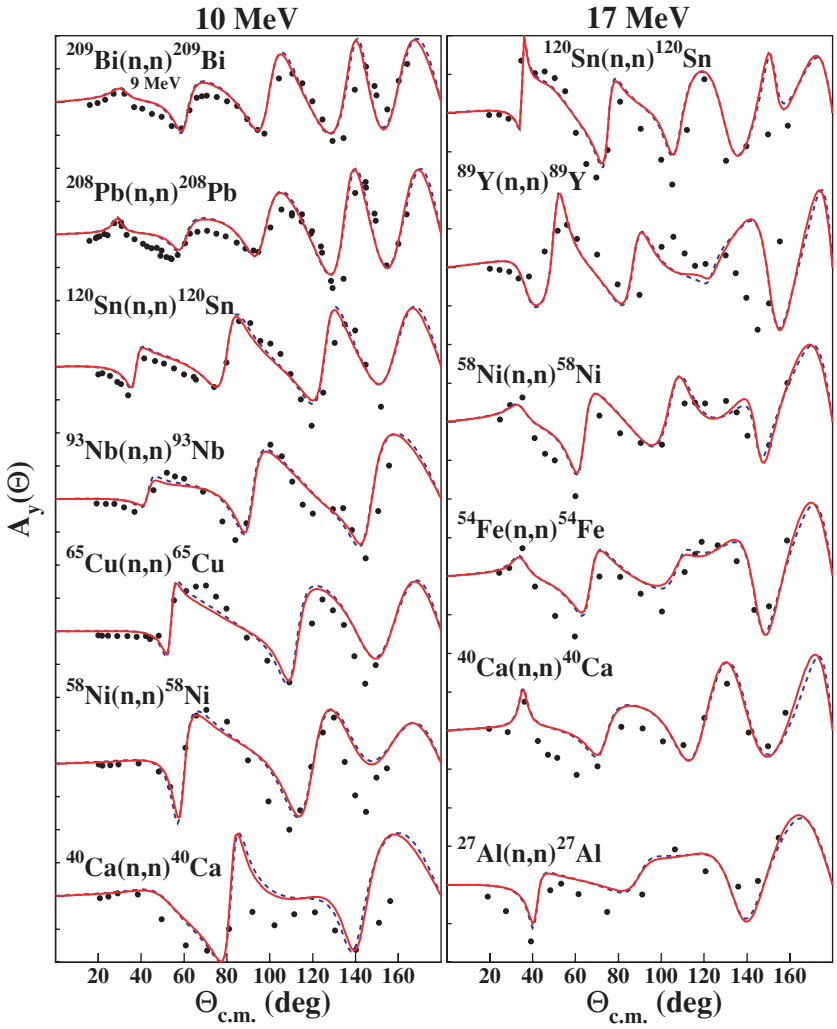

FIG. 1. (Color online) Comparison of analyzing powers and experimental data for 10- and 17-MeV neutrons scattered from ^{27}Al, ^{40}Ca, ^{58}Ni, ^{65}Cu, ^{54}Fe, ^{58}Ni, ^{89}Y, ^{93}Nb, ^{120}Sn, ^{208}Pb, and ^{209}Bi. The blue dotted line represents our neutron OMP [1] and the red solid line shows the results obtained with the modified spin-orbit potential (see Sec. IV).

the real part and the geometrical parameters (radius R and diffuseness a).

A. Imaginary potentials

The energy dependence of our surface imaginary neutron potential is

$$W_S^n(E) = \frac{A_S\left(E - E_F^n\right)^2}{\left(E - E_F^n\right)^2 + B_S^2} \exp\left[-C_S\left(E - E_F^n\right)\right], \quad (2)$$

where E_F^n denotes the neutron Fermi energy. The parameter A_S increases with the nuclear mass A ($A_S = -17 + 0.018A$) and the parameters C_S and B_S are constant. When we defined our neutron potential, we had not needed a $(N - Z)/A$ dependence to reproduce the experimental data because we were building a global optical potential for neutrons only. If we want to extend it for proton we have to include this isospin dependence (the Lane term [11,12]) in the A_S parameter. It was rather easy to fit the nuclear mass dependence of the A_S parameter on the isospin dependence and this led to a very good description of the neutron total and differential elastic cross sections. The expression of A_S is listed in Table I for neutrons. For protons, the modified expression of A_S listed in Table I cannot reproduce perfectly the experimental data. However, better results are obtained when the B_S parameter is increased and the C_S parameter decreases with the nuclear mass, as is shown in Table I.

When the volume imaginary potential (W_V) is modified, there are no many changes to the calculated cross sections, but a little improvement is observed for neutrons and protons when the B_V parameter (see the expression for W_V in Table I) is increased up to 25%. For the same reason the imaginary spin-orbit potential is reduced by a factor of 2. All the needed parameters and the energy dependencies to define the imaginary neutron and proton potentials noted "M.R.07a" are listed in Table I.

B. Real potentials

The real volume potential is the same for neutrons and protons with the exception of the Z/R term, which exists only for protons. A slight improvement is observed on the proton single-particle energies if the Z/R term is increased by 15%. The energy dependence and the parameters for the real volume as well as for the real spin-orbit potentials have been brought together with the imaginary potentials in Table I. Let us specify that E_F^n and E_F^p represent the Fermi energy for neutrons and protons, respectively. The last part of the real

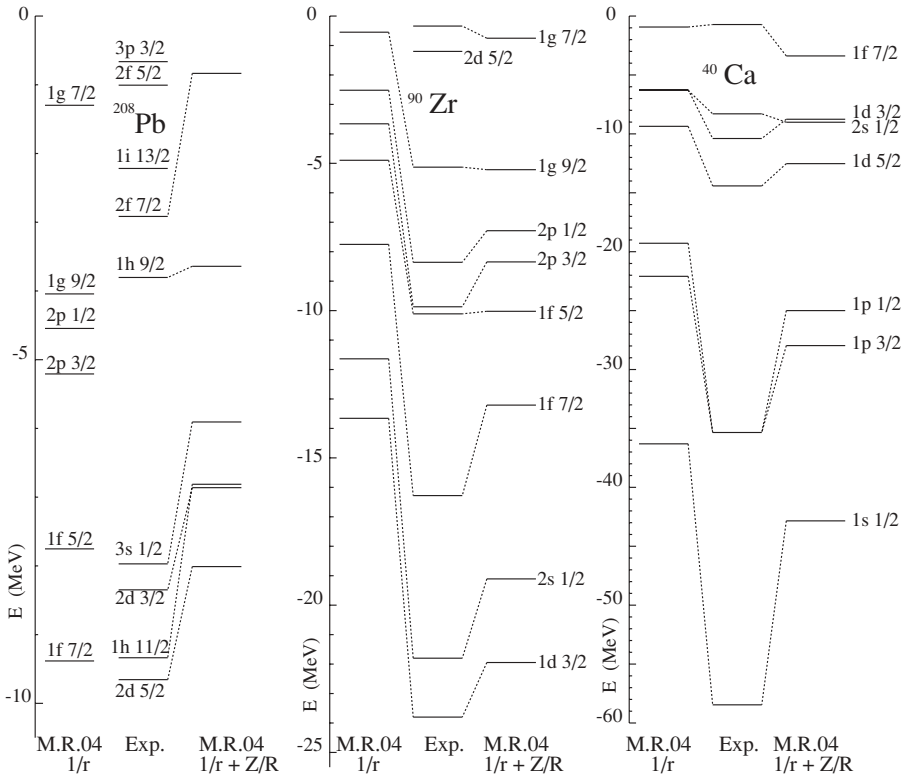

FIG. 2. Proton single-particle energies in ^{208}Pb, ^{90}Zr, and ^{40}Ca. For each nucleus, the first column displays the values calculated from our neutron potential including the Coulomb potential ("M.R.04 + 1/r"), the column labeled "Exp." displays the experimental values, and the third column shows the results when the Z/R term is added to the real volume potential ("M.R.04 + 1/r + Z/R").

potential comes from the imaginary volume (ΔV_V), surface (ΔV_S), and spin-orbit (ΔV_{SO}) potentials through the dispersion relation [2].

C. Geometrical parameters

The neutron and proton potentials share the same geometrical parameters (radius $R = r A^{1/3}$ and diffuseness a), which are mass dependent but independent of energy. To improve the quality of the fit to the data, the reduced radius is increased by 0.3% compared to the previous neutron potential [1]. Mass dependencies for the geometrical parameters are listed at the end of Table I.

D. Energy dependencies

Energy dependencies of the depths of the imaginary volume (W_V) and surface (W_S) potentials are shown in Fig. 5 for

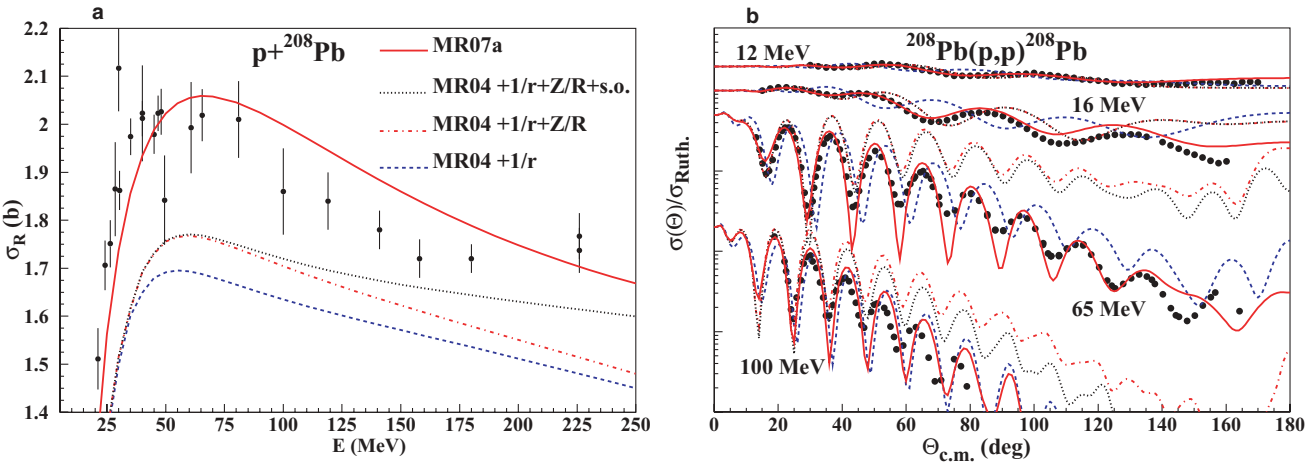

FIG. 3. (Color online) Proton reaction cross sections σ_R (left panel) and selected proton scattering cross sections on ^{208}Pb (right panel). Experimental data are shown by black circles. For the blue long-dashed lines, the neutron potential including the Coulomb potential ("M.R.04 + 1/r") is used; if the Z/R term is added to the real potential, we obtained the red dashed-dotted line ("M.R.04 + 1/r + Z/R"); the black dotted line shows the results when the new real spin-orbit potential is used ("M.R.04 + 1/r + Z/R + s.o."). The red solid line represents our final proton potential ("M.R.07a").

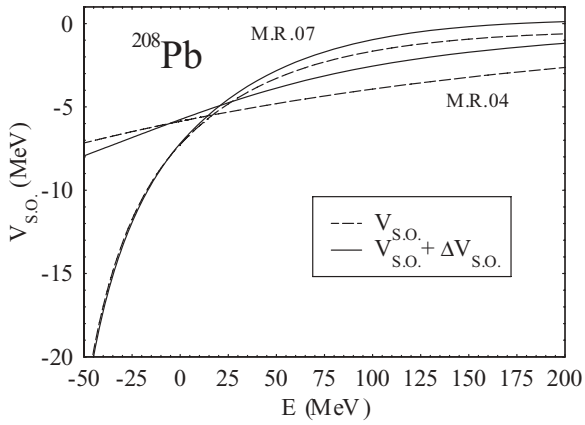

FIG. 4. Depths of spin-orbit real potential for ^{208}Pb. Curves labeled "M.R.04" represent our spin-orbit real potential used in 2004; those labeled "M.R.07" represent our spin-orbit potential with a local energy approximation. The solid curve gives the variation of the total spin-orbit potential and the dashed curve gives the variation without the dispersion contribution.

neutrons (upper panel) and protons (lower panel) for three nuclei: ^{32}S, ^{93}Nb, and ^{209}Bi. There are small differences between neutrons and protons for the imaginary volume potential owing to the Fermi energy. However, the surface imaginary potential of the heaviest nuclei is much deeper for the proton potential than for the neutron potential. For the lightest nuclei, the opposite is true. It was necessary to increase the surface imaginary potential for the heaviest nuclei

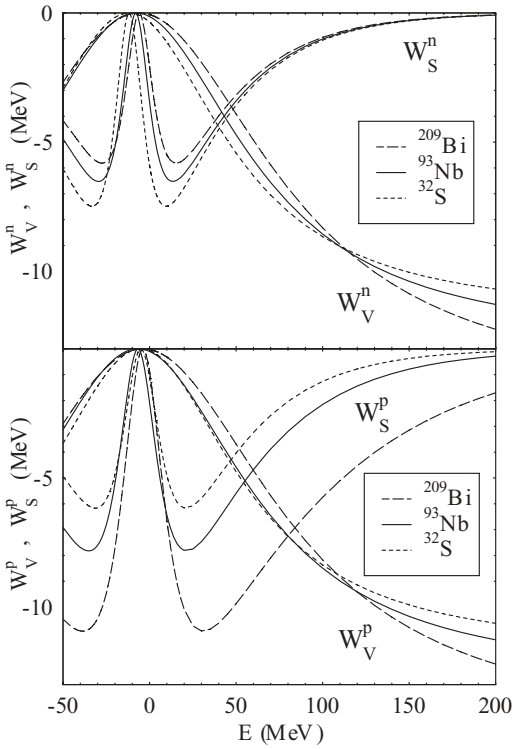

FIG. 5. Depths of neutron (upper panel) and proton (lower panel) volume $[W_V(E)]$ and surface $[W_S(E)]$ imaginary potentials for ^{32}S, ^{93}Nb, and ^{209}Bi.

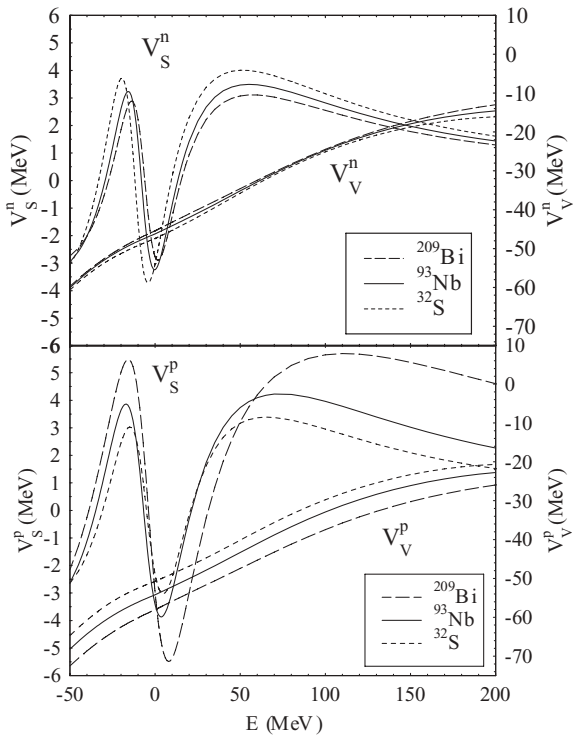

FIG. 6. Depths of neutron (upper panel) and proton (lower panel) volume $[V_V^n(E) = V_{\text{H.F.}}(E) + \Delta V_V^n(E),\ V_V^p(E) = V_{\text{H.F.}}(E) + \Delta V_V^p(E) + 1.15Z/R]$ and surface $[V_S(E) = \Delta V_S(E)]$ real potentials for ^{32}S, ^{93}Nb, and ^{209}Bi. The scale for the surface potential is on the left and that for the volume potential on the right.

to provide a good description of the proton differential elastic cross sections.

The depths of the real volume (V_V) and surface (V_S) potentials are represented in Fig. 6 between -50 and 200 MeV for neutrons (upper panel) and protons (lower panel) for the same three nuclei (^{32}S, ^{93}Nb, and ^{209}Bi). The volume potential contains the volume dispersive contribution ΔV_V when the surface potential represents directly the surface dispersive contribution $V_S = \Delta V_S$. The differences between nuclei for the surface part are due to the variations of the surface imaginary potentials for ^{32}S, ^{93}Nb, and ^{209}Bi. The only variation between neutrons and protons for the real volume potential is the Z/R term, which is much bigger for ^{209}Bi.

E. Volume integral

The volume integral and the root mean square (rms) radius are useful means of comparison between potentials. To calculate the volume integral per nucleon of the real potential, one must take into account all the real parts of the central potential $[V_V(E) + \Delta V_V(E) + \Delta V_S(E)]$. Let $[r^n](E)$ $(n = 2, 4)$ denote the radial moments:

$$[r^n](E) = -\frac{4\pi}{A}\int_0^\infty r^n[V_V(E) + \Delta V_V(E) + 4e^{\frac{r-R}{a}} f(r)\Delta V_S(E)]f(r)dr.$$

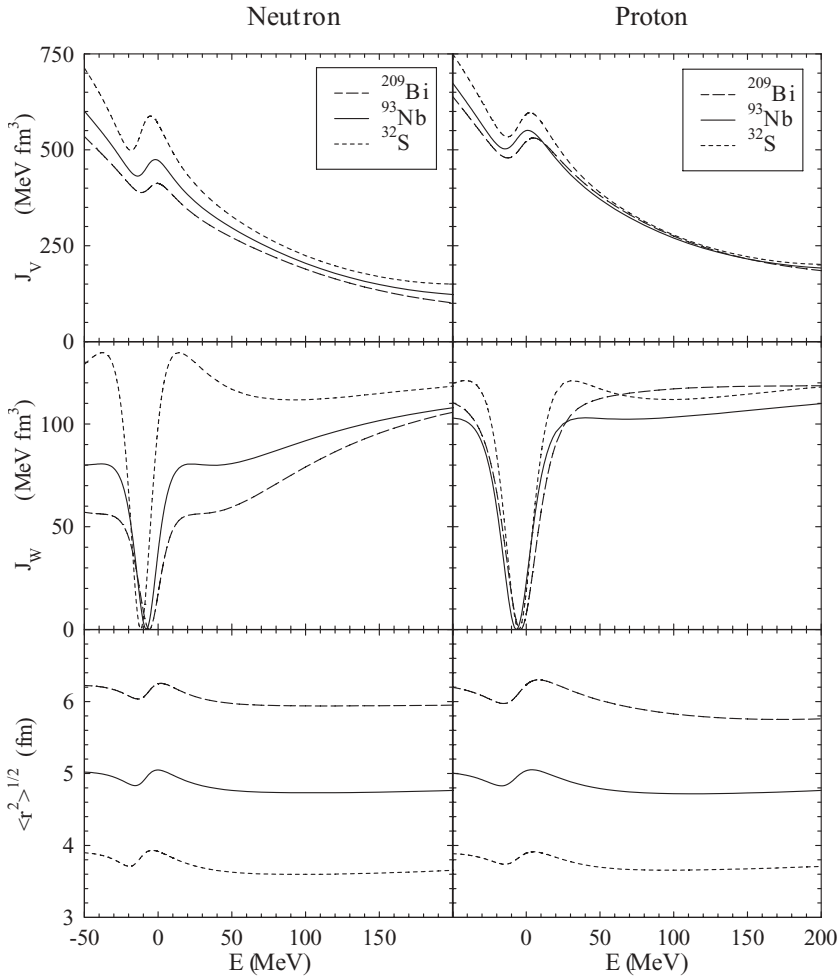

FIG. 7. Real (J_V) and imaginary (J_W) volume integrals per nucleon, and root mean square radius as functions of incident energy for neutrons (left panels) and protons (right panels). Each quantity is represented for ^{32}S (dotted lines), ^{93}Nb (solid lines), and ^{209}Bi (long-dashed lines).

The real volume integral per nucleon $J_V(E)$ is written

$$J_V(E) = [r^2](E),$$

the imaginary volume integral per nucleon $J_W(E)$ is given by

$$J_W(E) = -\frac{4\pi}{A}\int_0^\infty r^2[W_V(E) + 4e^{\frac{r-R}{a}} f(r)W_S(E)]f(r)dr,$$

and the rms radius is defined by

$$\sqrt{\langle r^2\rangle} = \sqrt{[r^4](E)/[r^2](E)}.$$

Energy dependencies of the volume integrals [$J_V(E)$ and $J_W(E)$] and of the rms radius for neutrons and protons are shown in Fig. 7 for ^{32}S, ^{93}Nb, and ^{209}Bi. Similar dependencies have also been observed for neutrons or protons on ^{208}Pb, ^{90}Zr, and ^{40}Ca. [9,13,14].

F. Lane-consistent optical model potential

Our global optical model is not Lane-consistent even though it contains $(N - Z)/A$ dependence in the imaginary surface part. To build such a potential, we keep the same parameters $B_S = 13$ and $C_S = 0.025$ for protons and neutrons. To reproduce the proton experimental data, we decided to seek a different volume imaginary potential.

As we did for the surface imaginary neutron potential, we try to include an isospin dependence in the A_V and B_V parameters for the volume imaginary neutron potential:

$$W_V^n(E) = \frac{A_V\left(E - E_F^n\right)^2}{\left(E - E_F^n\right)^2 + B_V^2}.$$

The new parameters $A_V = -11 - 16(N - Z)/A$ and $B_V = 65 + 120(N - Z)/A$ can reproduce neutron scattering data but unfortunately, when we use an isospin dependence for the proton [$A_V = -11 + 16(N - Z)/A$ and $B_V = 65$–$120(N - Z)/A$], the agreement between predictions and experimental data is poor. A big improvement is observed for protons if we keep the original mass dependency for the A_V parameter ($A_V = -11.21 - 0.017A$) and choose an isospin dependence for the B_V parameter [$B_V = 65$–$120(N - Z)/A$]. At the same time, the imaginary spin-orbit potential is slightly modified to obtain better results. Finally, we succeeded in building a Lane-consistent imaginary surface potential and we failed for the imaginary volume potential. All the needed parameters and the energy dependencies to define the imaginary neutron and proton potentials are listed in Table II. This potential is denoted "M.R.07b".

Energy dependencies of the depths of the imaginary volume (W_V) and surface (W_S) proton potentials are shown in Fig. 8 (upper panel) for the same three nuclei (^{32}S, ^{93}Nb, and ^{209}Bi).

TABLE II. Energy dependencies and parameters for imaginary part of the potential "M.R.07b." The real part and the geometrical parameters are given in Table I.

$W_S^{n,p}(E) = \frac{A_S(E-E_F^{n,p})^2}{(E-E_F^{n,p})^2+B_S^2} \exp[-C_S(E-E_F^{n,p})]$		
	neutron	proton
A_S	$-17.5+19\frac{N-Z}{A}$	$-17.5-19\frac{N-Z}{A}$
B_S	13	
C_S	0.025	
$W_V^{n,p}(E) = \frac{A_V(E-E_F^{n,p})^2}{(E-E_F^{n,p})^2+B_V^2}$		
	neutron and proton	
A_V	$-11.21-0.017A$	
	neutron	proton
B_V	$65+120\frac{N-Z}{A}$	$65-120\frac{N-Z}{A}$
$W_{SO}^{n,p}(E) = \frac{-1.25(E-E_F^{n,p})^2}{(E-E_F^{n,p})^2+50^2}$		
	neutron and proton	

The proton imaginary surface potential is still deeper for the heaviest nuclei but the differences are much smaller among the nuclei. However, there are big differences among nuclei for the imaginary volume potential. The depths of the real volume $(V_V + \Delta V_V)$ and surface $(V_S = \Delta V_S)$ proton potentials are represented in Fig. 8 (lower panel) between −50 and 200 MeV. The differences among nuclei for the real surface potential are small owing to the slight variations of the imaginary surface potentials. The deviation on the real volume proton potential around zero MeV is due to the dispersive volume contribution and is deeper for heavy nuclei.

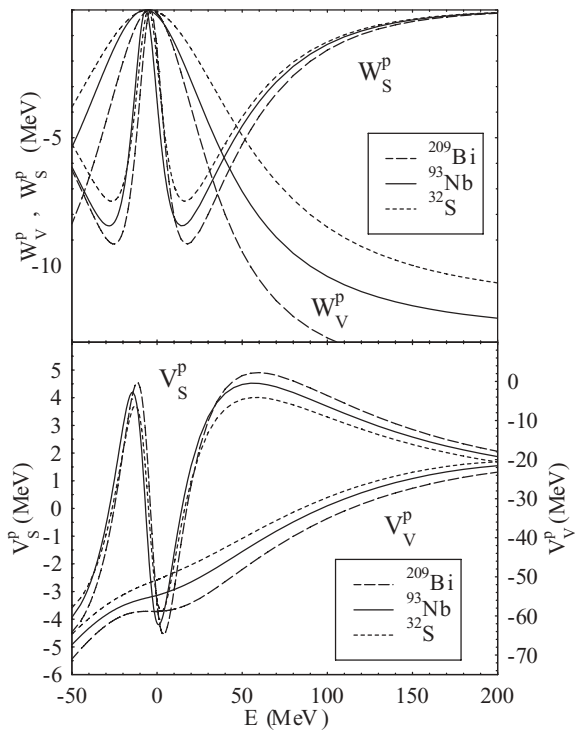

FIG. 8. Depths of imaginary (upper panel) and real (lower panel) proton potentials "M.R.07b" for ^{32}S, ^{93}Nb, and ^{209}Bi.

The needed parameters to define the new surface and volume imaginary potentials are listed in Table II.

V. PROTON REACTION AND DIFFERENTIAL CROSS SECTIONS

The nonlocal, dispersive, and spherical neutron and proton optical model "M.R.07a" is completely defined with the parameters of Table I whereas the potential "M.R.07b" is defined with the parameters of Table II. The reaction cross section (left panel) and selected elastic angular distributions (right panel) for protons on ^{208}Pb calculated with the OMP labeled "M.R.07a" (red solid curves) are compared with experimental data (black circles) in Fig. 3. However, the calculated reaction cross section overestimates the data between 100 and 200 MeV. That is the price paid to reproduce the differential elastic cross sections at higher energies. Our proton OMP has also been used to predict reaction cross sections σ_R, angular distributions $\sigma(\theta)/\sigma_{\text{Ruth.}}$, and analyzing powers $A_y(\theta)$ for many nuclei, and comparisons between experimental data and the calculations are shown in Figs. 9, 10, and 11. An overall good description of the reaction cross section is obtained. Some deviations occur for the minima of the angular distributions and it should be noted that there is poor agreement between predictions and experimental data for ^{40}Ca. The predicted analyzing powers are in good agreement with experimental data below 100 MeV whereas above this energy there is a poor description of $A_y(\theta)$.

We did not show comparisons on diffusion data between our past neutron potential "M.R.04" and our new neutron potentials "M.R.07a" or "M.R.07b" because there are only minor differences for neutron total and differential calculated cross sections.

VI. SINGLE-PARTICLE ENERGIES

We next compare the neutron bound single-particle states obtained from the neutron OMP defined in Table I with our previous OMP [1]. As can be seen in Fig. 4, the new real spin-orbit potential is very different than the potential published in 2004 for negative energy. The neutron single-particle and hole states of ^{208}Pb, ^{90}Zr, and ^{40}Ca predicted with these two OMPs are compared with experimental values in Fig. 12. Results are slightly better for the new potential for ^{40}Ca, ^{208}Pb, and ^{90}Zr.

In Fig. 13, the proton single-particle and hole states of ^{208}Pb, ^{90}Zr, and ^{40}Ca calculated with our proton OMP are compared with experimental data. The results obtained with our proton OMP, labeled "M.R.07a" in this figure, are in good agreement with the experimental data for the three nuclei. There is only a large discrepancy for the deepest state of ^{40}Ca. The results obtained with the Rost [8], the Wang *et al.* [9], and the Tornow [10] potentials are also shown in Fig. 13 for ^{208}Pb, ^{90}Zr, and ^{40}Ca, respectively. Rost built a shell-model potential for lead, and Wang *et al.* and Tornow used a dispersive OMP to calculate scattering data of protons on ^{90}Zr and ^{40}Ca, respectively, and extended it to negative energy. The OMP of Rost, Wang *et al.*, and Tornow perform slightly better than our OMP but those potentials are devoted to one nucleus whereas our new potential predicts cross sections and single-particle

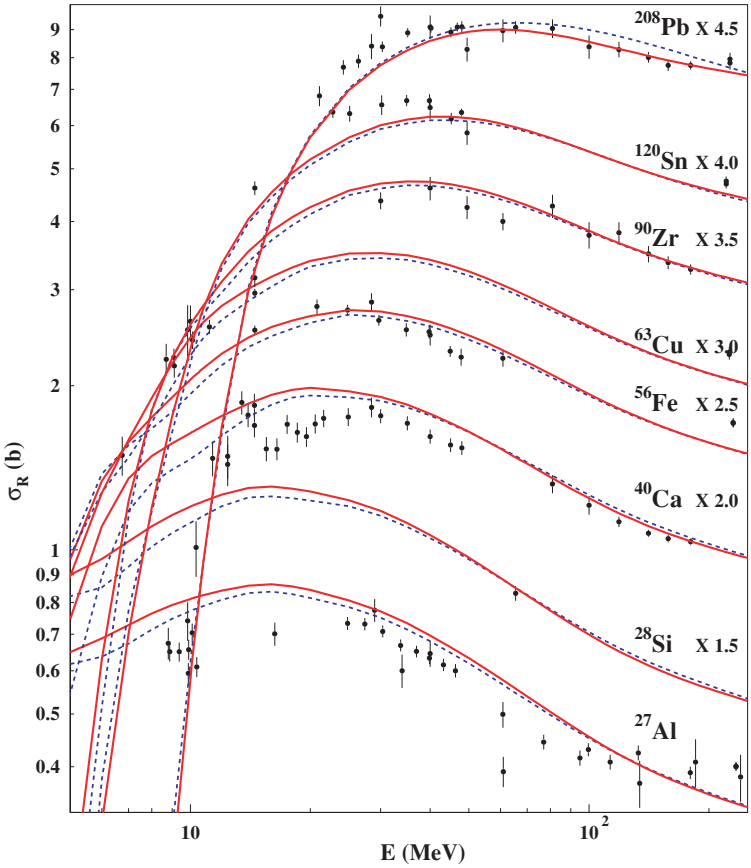

FIG. 9. (Color online) Comparison of calculated proton reaction cross sections and experimental data for nuclides in the Al–Pb mass region. The curve and the data points for ^{27}Al represent the true values; the others are offset by factors of 1.5, 2, 2.5, 3, 3.5, 4, and 4.5. The blue dotted lines represent the calculated reaction cross sections with the "M.R.07a" OMP and the red solid lines show the results obtained with the "M.R.07b" OMP.

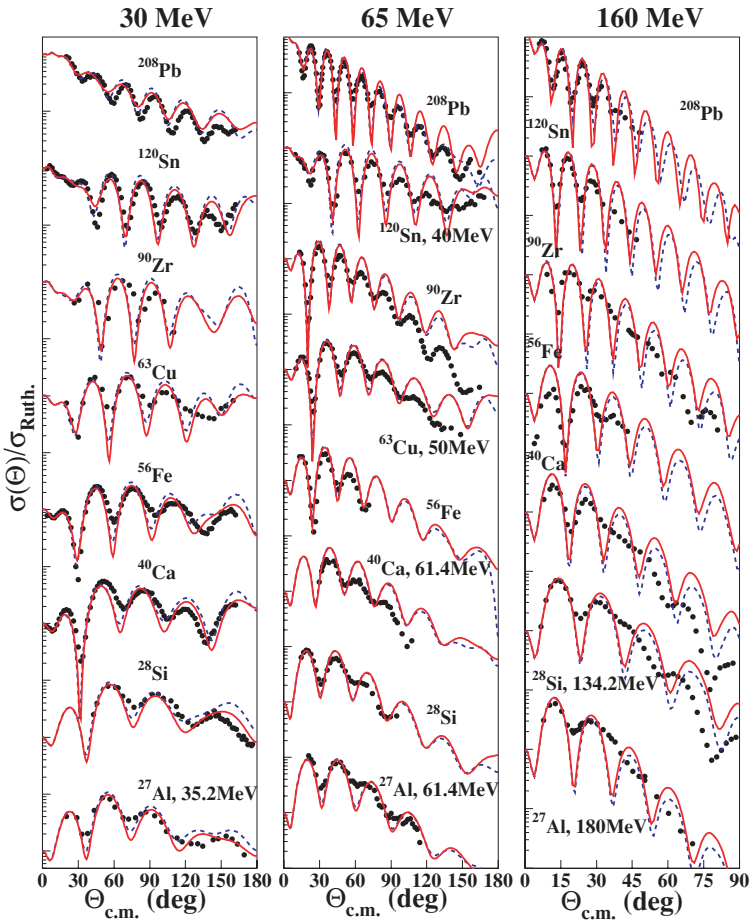

FIG. 10. (Color online) Comparison of calculated proton scattering cross sections and experimental data for nuclides in the Al–Pb mass region. The blue dotted lines represent the calculated scattering cross sections with the "M.R.07a" OMP and the red solid lines show the results obtained with the "M.R.07b" OMP.

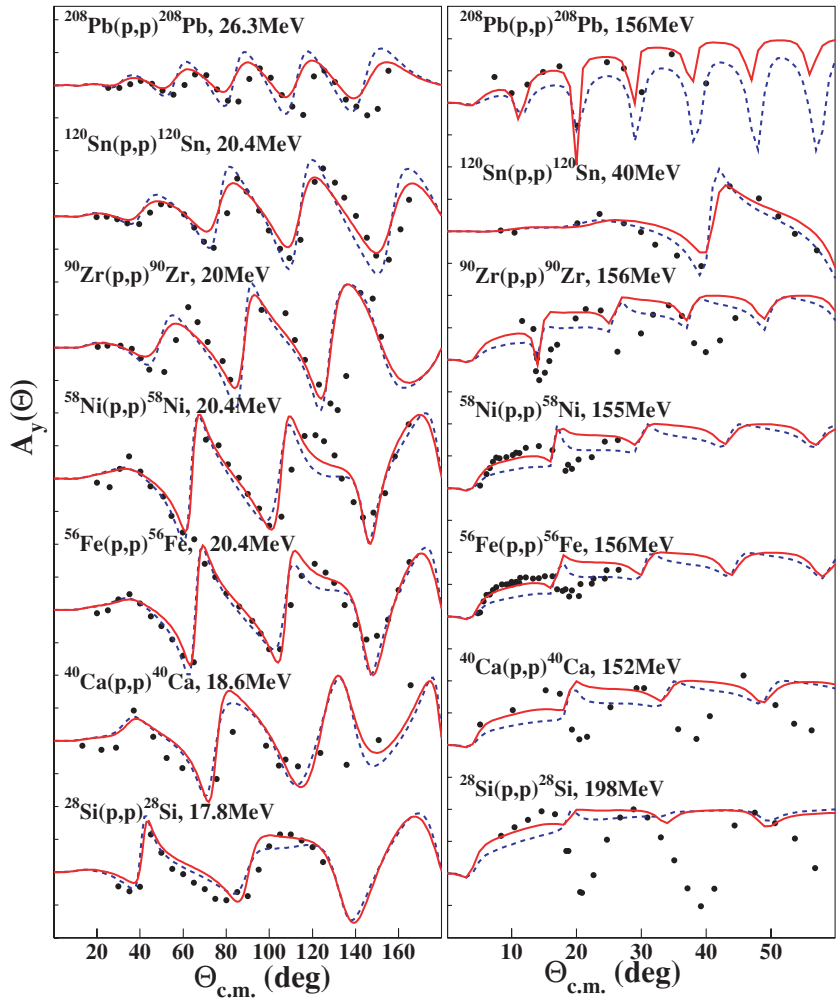

FIG. 11. (Color online) Comparison of calculated proton analyzing powers and experimental data for nuclides in the Al–Pb mass region. The blue dotted lines represent the calculated analyzing powers with the "M.R.07a" OMP and the red solid lines show the results obtained with the "M.R.07b" OMP.

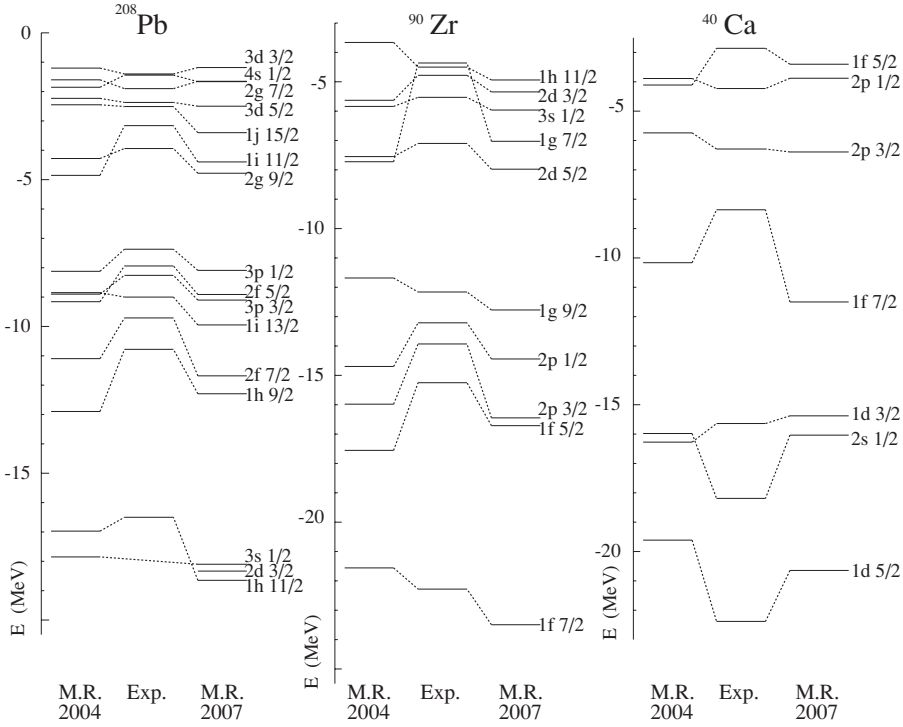

FIG. 12. Neutron single-particle energies in ^{208}Pb, ^{90}Zr, and ^{40}Ca. For each nucleus, the first column displays the values calculated from our previous neutron OMP ("M.R.2004"), the column labeled "Exp." displays the experimental values, and the third column shows the results obtained with the neutron OMP defined in Table I.

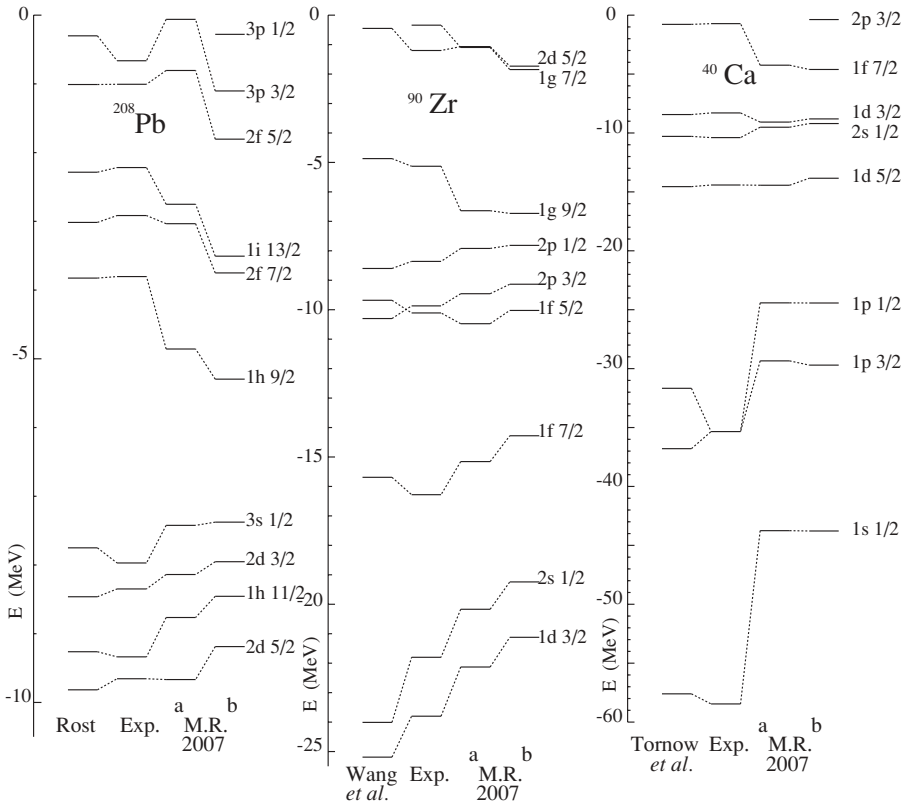

FIG. 13. Proton single-particle energies. The first column shows the results obtained with the Rost potential [8], the Wang potential [9], and the Tornow potential [10] in ^{208}Pb, ^{90}Zr, and ^{40}Ca, respectively. For each nucleus, the last column displays the values calculated from the OMP "M.R.07b," the third column shows the results obtained with the OMP "M.R.07a", and the column labeled "Exp." shows the experimental values.

energies for neutrons and protons and for all spherical nuclei. The predictions calculated with the "M.R.07b" OMP are also shown in Fig. 13. Agreement with the experimental values is not as good as with the "M.R.07a" potential for ^{208}Pb and ^{90}Zr.

From the proton solution U^p_{nlj} of the radial Schrödinger equation, it is possible to calculate the charge densities ρ_C in the spherical shell-model basis for a closed-shell configuration:

$$\rho_C(r) = \sum_{\substack{\text{occupied}\\ nlj}} \frac{2j+1}{4\pi} \left| \frac{U^p_{nlj(r)}}{r} \right|^2 .$$

The experimental charge densities for ^{40}Ca, ^{90}Zr, and ^{208}Pb [15] are shown in Fig. 14 by red squares, black circles, and blue triangles, respectively. In the same figure, we compare the experimental data and the calculated charge densities obtained with our OMP including dispersion relations and the local energy approximation of Perey-Buck (red solid and dotted lines for ^{40}Ca, black solid and dotted lines for ^{90}Zr, and blue solid and dotted lines for ^{208}Pb). The dotted lines represent the charge-density distributions calculated with the "M.R.07a" OMP and the solid lines show the results obtained with the "M.R.07b" OMP. There is poor agreement between theory and experiment for the three nuclei, although better results are obtained with the "M.R.07b" potential. A large improvement is obtained if we increase the radius of the nuclei, but in this case we lose the nice agreement with the experimental scattering data.

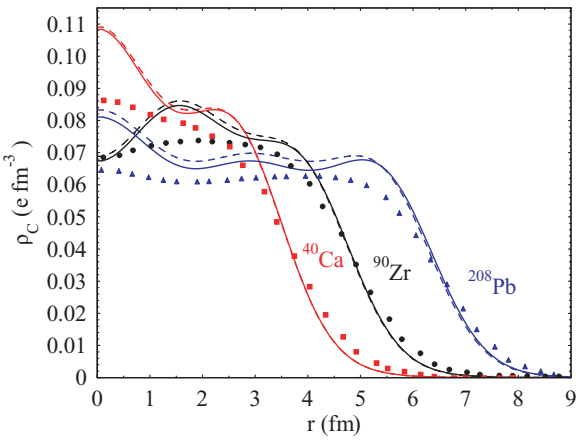

FIG. 14. (Color online) Experimental charge-density distributions compared with those calculated with our proton OMP (the blue triangles, solid and dotted lines; the black circles, solid and dotted lines; and the red squares, solid and dotted lines, refer to ^{208}Pb, ^{90}Zr, and ^{40}Ca, respectively). The dotted lines represent the charge-density distributions calculated with the "M.R.07a" OMP whereas the solid lines show the results obtained with the "M.R.07b" OMP.

VII. CONCLUSIONS

In this work, we have built a global OMP for incident neutrons and protons on spherical nuclei that contains dispersion relations and the local energy approximation of Perey and Buck. This potential, which is very close to our previous neutron potential recently published, provides a very good description of the neutron total and differential elastic cross

sections. For negative energies, this potential provides a reasonably good description of bound single-particle states for neutrons and protons. For the scattering of protons, the situation is not as satisfactory as for neutrons, probably because we tried to extend a neutron potential to protons. Nevertheless, this analysis shows that it is possible to reproduce nucleon cross sections and bound states for spherical nuclei with very simple functional forms owing to the dispersion relations and the local energy approximation. The main difference between the neutron and proton nuclear potential rests in the surface imaginary term for the "M.R.07a" OMP and in the volume imaginary term for the "M.R.07b" OMP.

To obtain an agreement between experimental and calculated data for protons as good as for neutrons, it would be necessary to seek the parameters of the global optical model simultaneously for protons and neutrons. But would it be possible to reproduce the experimental charge-density without destroying the diffusion observables?

[1] B. Morillon and P. Romain, Phys. Rev. C **70**, 014601 (2004).
[2] C. Mahaux, H. Ngô, and G. R. Satchler, Nucl. Phys. **A449**, 354 (1986).
[3] F. G. Perey and B. Buck, Nucl. Phys. **32**, 353 (1962).
[4] B. Morillon and P. Romain, Phys. Rev. C **74**, 014601 (2006).
[5] G. E. Brown and M. Rho, Nucl. Phys. **A372**, 397 (1981).
[6] J. Raynal, Notes on ECIS94, CEA Saclay Report No. CEA-N-2772, 1994 (unpublished).
[7] F. G. Perey, Phys. Rev. **131**, 745 (1963).
[8] E. Rost, Phys. Lett. **B26**, 184 (1968).
[9] Y. Wang, C. C. Foster, R. D. Polak, J. Rapaport, and E. J. Stephenson, Phys. Rev. C **47**, 2677 (1993).
[10] W. Tornow, Z. P. Chen, and J. P. Delaroche, Phys. Rev. C **42**, 693 (1990).
[11] A. M. Lane, Phys. Rev. Lett. **8**, 171 (1962).
[12] A. M. Lane, Nucl. Phys. **35**, 676 (1962).
[13] C. H. Johnson, D. J. Horen, and C. Mahaux, Phys. Rev. C **36**, 2252 (1987).
[14] C. H. Johnson and C. Mahaux, Phys. Rev. C **38**, 2589 (1988).
[15] W. A. Richter and B. A. Brown, Phys. Rev. C **67**, 34317 (2003).